SCIENCE CHINA
Physics, Mechanics & Astronomy

•Article•

September 2021 Vol. 64 No. 9: 294211
https://doi.org/10.1007/s11433-020-1682-1

Chip-compatible wide-field 3D nanoscopy through tunable spatial frequency shift effect

Xiaowei Liu[1,2†], Mingwei Tang[1†], Chao Meng[1], Chenlei Pang[2], Cuifang Kuang[1], Wei Chen[1,3], Clemens F. Kaminski[4], Qing Yang[1,2*], and Xu Liu[1,2*]

[1] *State Key Lab of Modern Optical Instrumentation, College of Optical Science and Engineering, International Research Center for Advanced Photonics, Zhejiang University, Hangzhou 310058, China;*
[2] *Research Center for Inteligent Sensing, Zhejiang Lab, Hangzhou 311100, China;*
[3] *Department of Cell Biology, Department of Cardiology of the Second Affiliated Hospital, School of Medicine, Zhejiang University, Hangzhou 310058, China;*
[4] *Department of Chemical Engineering and Biotechnology, University of Cambridge, Cambridge CB30AS, UK*

Received November 24, 2020; accepted February 22, 2021; published online April 12, 2021

Spatial frequency shift (SFS) microscopy with evanescent wave illumination shows intriguing advantages, including large field of view (FOV), high speed, and good modularity. However, a missing band in the spatial frequency domain hampers the SFS superresolution microscopy from achieving resolution better than 3 folds of the Abbe diffraction limit. Here, we propose a novel tunable large-SFS microscopy, making the resolution improvement of a linear system no longer restricted by the detection numerical aperture (NA). The complete wide-range detection in the spatial frequency domain is realized by tuning the illumination spatial frequency actively and broadly through an angle modulation between the azimuthal propagating directions of two evanescent waves. The vertical spatial frequency is tuned via a sectional saturation effect, and the reconstructed depth information can be added to the lateral superresolution mask for 3D imaging. A lateral resolution of $\lambda/9$, and a vertical localization precision of $\sim\lambda/200$ (detection objective NA = 0.9) are realized with a gallium phosphide (GaP) waveguide. Its unlimited resolution enhancing capability is demonstrated by introducing a designed metamaterial chip with an unusual large refractive index. Besides the great resolution enhancement, this method shows better anti-noise capability than classical structured illumination microscopy without SFS tunability. This method is chip-compatible and can potentially provide a mass-producible illumination chip module achieving the fast, large-FOV, and deep-subwavelength 3D nanoscopy.

superresolution, spatial frequency shift, evanescent wave, wide-field microscopy, chip-compatible microscopy

PACS number(s): 42.30.Lr, 42.30.Wb, 42.82.Et

Citation: X. Liu, M. Tang, C. Meng, C. Pang, C. Kuang, W. Chen, C. F. Kaminski, Q. Yang, and X. Liu, Chip-compatible wide-field 3D nanoscopy through tunable spatial frequency shift effect, Sci. China-Phys. Mech. Astron. **64**, 294211 (2021), https://doi.org/10.1007/s11433-020-1682-1

1 Introduction

The development of 3D superresolution microscopy has dramatically benefited the current scientific studies at the subwavelength scale. Generally speaking, there are two groups of 3D superresolution techniques. The first group includes single-molecule localization microscopy, stimulated emission depletion microscopy, confocal microscopy, multiphoton microscopy, etc. [1-9], which squeezes the point spread function in the space domain and uses sequential

*Corresponding authors (Qing Yang, email: qingyang@zju.edu.cn; Xu Liu, email: liuxu@zju.edu.cn)
†These authors contributed equally to this work.

© Science China Press and Springer-Verlag GmbH Germany, part of Springer Nature 2021

blinking or raster scan to achieve the full landscape of an object. Its resolution could reach tens of nanometers while the speed has been restricted by the point-by-point precise scanning process or the requirement of hundreds of pictures. The second group broadens the detection range in the spatial frequency domain through the SFS effect, whose imaging speed is high due to the wide-field implementation [10-12]. To enable SFS microscopy with a superresolution at the subwavelength scale, it is essential to use the near-field evanescent wave with a higher wave vector than the far-field propagation wave for illumination, which can be coincidentally built on the integrated photonics, paving the way for compact nanoscopy on a thin chip [13-20]. In the past several years, SFS superresolution microscopy has been proven with intriguing advantages, including high speed, large FOV, and good modularity. In 2017, we reported the chip-based label-free SFS superresolution microscopy with a FOV 1-2 magnitude larger than the other wide-field label-free superresolution techniques [13,21,22]. Very recently, chip-based label-free SFS superresolution microscopy integrated with polymer films [14] and chip-based structured illumination microscopy [17] were published, making the SFS method mass-productive and stable.

However, the lack of an approach to actively tune the SFS in a large range hampers the progress to achieve deep-subwavelength resolution through evanescent illumination with ultra-large wave vectors [23-25]. When the wave vector of the illumination surpasses two folds of the cutoff frequency of the objective, a missing band exists between the shifted components and the zeroth component in the spatial frequency domain, as shown in Figure 1(a), which causes severe artifacts and distortion in the image (middle bottom in Figure 1(b)), and thus restricts the resolution below triple of the Abbe diffraction limit of the detection system [26,27].

In this paper, we propose a chip-compatible 3D nanoscopy based on a tunable large-SFS effect, in which the resolution can be freely improved using an illumination chip of high effective refractive index, without a theoretical limit. In the lateral dimension, the SFS tunability is realized by modulating the azimuthal propagation direction of two evanescent waves, and the effective wave vector of their superposition can be tuned actively and broadly to enable a wide-range and complete detection in the spatial frequency domain, which is necessary to achieve an undistorted superresolution image with the theoretical high resolution (right bottom in Figure 1(b)). In the vertical dimension, we introduce a sectional saturation effect by intensity modulation to tune the vertical spatial frequency spectrum of the evanescent illumination so as to solve the vertical spatial distribution within the evanescent penetration depth. Finally, a 3D superresolution image can be achieved by multiplying the lateral and vertical distribution together.

This proposed 3D large frequency shift tuning method is compatible with chip waveguides. The wide-field properties of both the illumination and image capture process make the method possess high speed and large FOV. The use of evanescent illumination with large and tunable wave vectors provides the 3D deep-subwavelength resolution. We call this method the SFS tunable nanoscopy (STUN). Theoretically, the resolution can be significantly improved by introducing a waveguide material with an ultra-large effective refractive index in the STUN. In our following illustrations on the 3D STUN method, we select GaP as the waveguide material, considering its high refractive index and low optical loss in the visible spectrum [28,29]. A lateral resolution of $\lambda/9$, which is five folds of the diffraction-limited resolution, and a vertical localization precision of $<\lambda/200$ are achieved (detection objective NA = 0.9). Because of this SFS tunability, there is no longer a theoretical limitation on the resolution of a linear system. For example, when we use a metal-dielectric multilayered metamaterial supporting a mode effective refractive index up to 7.2, a lateral resolution of $\lambda/18$ and a vertical localization precision of $<\lambda/1000$ can be achieved without distortion. To perceive the practical case, we study the performance of STUN with Poisson noise added to each raw image. We find that STUN shows better anti-noise capability than the classical structured illumination microscopy (SIM), and the final 3D image can be reconstructed even when the peak photon number is 100 in each raw image. We anticipate this method can provide a mass-producible and robust chip module endowing a standard microscope with fast, large FOV and 3D deep-subwavelength resolving capability, which would benefit biological and clinical researches such as observing cytoskeleton dynamics [30] or vesicle trafficking during endocytosis/exocytosis [31].

2 Mechanism

2.1 Tunable large-SFS effect in the lateral dimension

To avoid the missing band in large-SFS imaging under evanescent illumination of large wave vector, the shift value needs to be tuned broadly. Through wave vector manipulation based on interfering two evanescent waves propagating along the different azimuthal directions, the superposed wave vector can be tuned broadly, which is determined by the sine of the half angle between the two propagation directions (equation shown in Figure 1(c)). The spatial frequency components that can be detected with the tunability of the illumination wave vector are illustrated in Figure 1(c). We have performed experiments using GaP crystal to show the tunability of the effective wave vector of the illumination. A 639-nm laser is coupled into the GaP crystal through a normal incidence on a designed grating, and the evanescent waves can be generated on the other side. The wave vector and direction of the evanescent wave are controlled by fab-

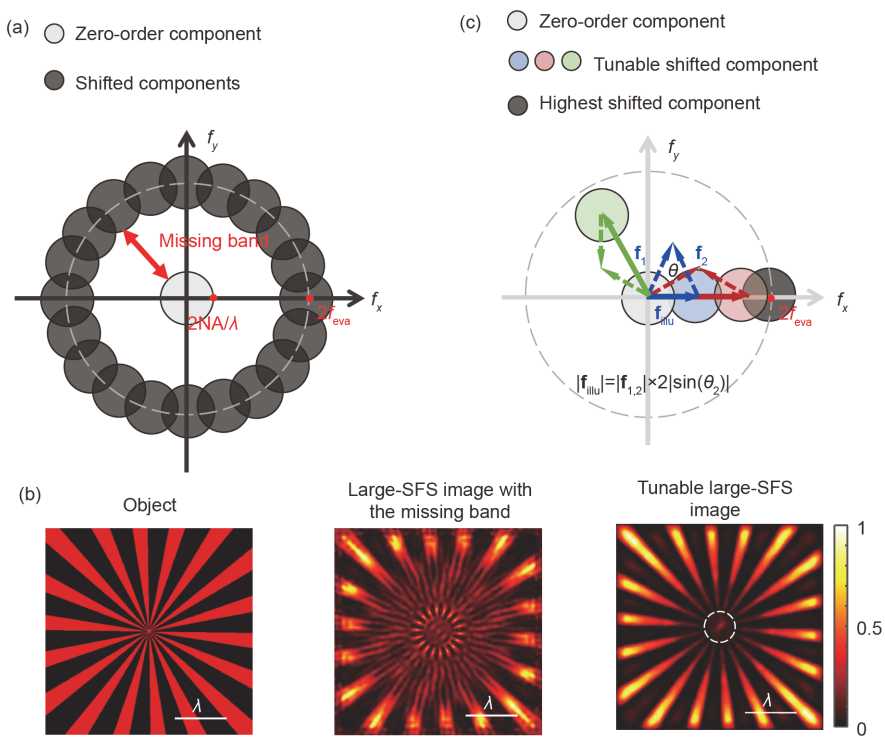

Figure 1 (Color online) Comparison between the large-SFS microscopy with and without the missing band in the spatial frequency domain and the illumination wave vector tuning mechanism. (a) Detected spatial frequency range when the spatial frequency of illumination (denoted as $2f_{\mathrm{eva}}$) is larger than two folds of the cutoff frequency of the objective. (b) Left bottom: object; middle bottom: reconstructed images in large-SFS condition with the missing band; right bottom: reconstructed image in tunable large-SFS condition with a complete coverage in the spatial frequency domain. The maximum SFS magnitude is 3.6. Objective NA = 0.9. The white dash line marks the position corresponding to a resolution of 0.11λ calculated by $0.5\lambda/(3.6+0.9)$. (c) Relationship between the SFS vector ($\mathbf{f}_{\mathrm{illu}}$, solid arrow) and the lateral wave vectors ($2\pi\mathbf{f}_1$ and $2\pi\mathbf{f}_2$, dash arrrow) of two evanescent waves that are used in interference for illumination. $\mathbf{f}_1$ and $\mathbf{f}_2$ are the lateral wave vectors of the evanescent waves devided by 2π. θ denotes the angle between $\mathbf{f}_1$ and $\mathbf{f}_2$. Blue, red, and green arrows represent three different superposition conditions, corresponding to different detected components (blue, red and green circles).

ricating grating with proper period and direction. In our experiments, evanescent waves with a lateral wave vector of $1.28\times2\pi/\lambda$ are generated. Figure 2 shows the interference pattern of two evanescent waves with 180°, 120°, and 60° between their wave vectors. The period of the pattern has been tuned from 0.38λ (241 nm) to 0.78λ (496 nm), very close to the theoretical calculations based on Figure 1(c).

This tuning approach does not affect the penetration depth of the evanescent illumination, which is vital for reliable image reconstruction. Based on this tuning mechanism, we designed a GaP waveguide chip with 10 input directions as shown in Figure 3(a), to achieve a reconstructed SFS image without the missing band in the spatial frequency domain (effective refractive index of the mode = 3.38; λ_{illu} = 561 nm, NA = 0.9). Light passes through rectangular waveguides into a decagon region, and the interference between optical modes from two rectangular waveguides creates a structured evanescent illumination for an object atop the waveguide surface. The rectangular waveguides are tens of micrometers in width, so the input modes barely diverge in the polygonal region (sect. 1 in Supplementary Information). The diameter of the FOV (red dashed circle in Figure 3(a)) is equal to the width of the rectangular waveguide, rather than determined by a far-field illumination objective. In the following text, n_{eff} represents the effective refractive index of the waveguide mode; I_{illu} and I_{emis} represent the illumination and emission intensity, respectively; λ_{illu} and λ_{emis} represent the illumination and emission wavelength, respectively. The intensity distribution of the interference pattern I_{illu} can be illustrated as:

$$I_{\mathrm{illu}}(\mathbf{r}) = A_1(\mathbf{r})^2 + A_2(\mathbf{r})^2 + 2A_1(\mathbf{r})A_2(\mathbf{r}) \times\cos\left[2\pi(\mathbf{f}_1-\mathbf{f}_2)\cdot\mathbf{r}+\Delta\phi\right], \quad (1)$$

where $A_1(\mathbf{r})$ and $A_2(\mathbf{r})$ represent the amplitudes of the two input modes; $2\pi\mathbf{f}_1$ and $2\pi\mathbf{f}_2$ represent their propagation wave vectors; $\Delta\phi$ represents their phase difference $|\mathbf{f}_1|=|\mathbf{f}_2|=n_{\mathrm{eff}}/\lambda_{\mathrm{illu}}$. The third term in eq. (1) represents a modulated illumination pattern whose wave vector is related to the sine of the half angle between the two input propagation wave vectors and thus can be tuned flexibly by changing the azimuthal incidence direction of the input modes in the SFS waveguide chip. Figure 3(b) and (c) show examples of the modulation of the illumination period and direction through wave vector manipulation by selecting different input ports on. The wave

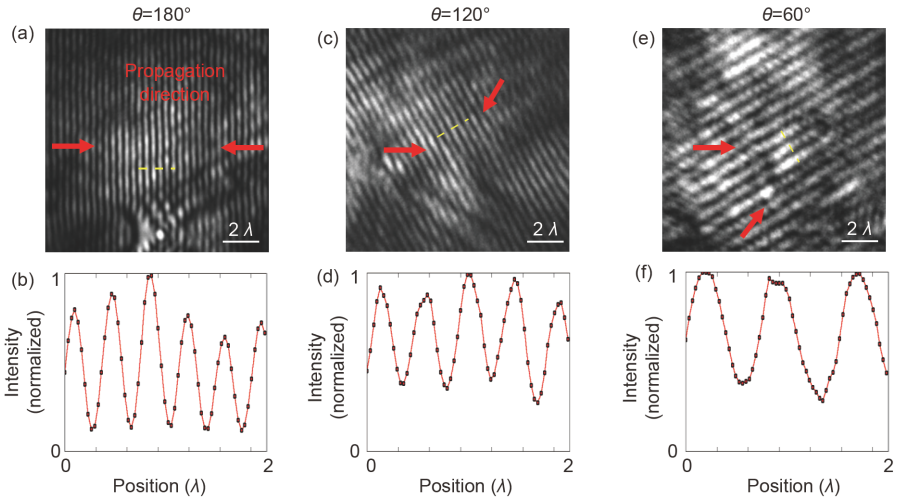

Figure 2 (Color online) Experimental demonstration on the tunability of the illumination wave vector. (a) The observed interference pattern of two evanescent waves with a 180° angle between their wave vectors. The red arrows indicate the propagation directions of the two evanescent waves. (b) The intensity profile plotted along the yellow dash line in (a). The period of the pattern is 0.38λ. (c)-(f) The observed interference pattern of two evanescent waves with 120° and 60° between their wave vectors and the corresponding intensity profiles. The periods in (d) and (f) are 0.44λ and 0.78λ, respectively. The lateral wave vector of the evanescent wave is $1.28\times2\pi/\lambda$, λ = 639 nm.

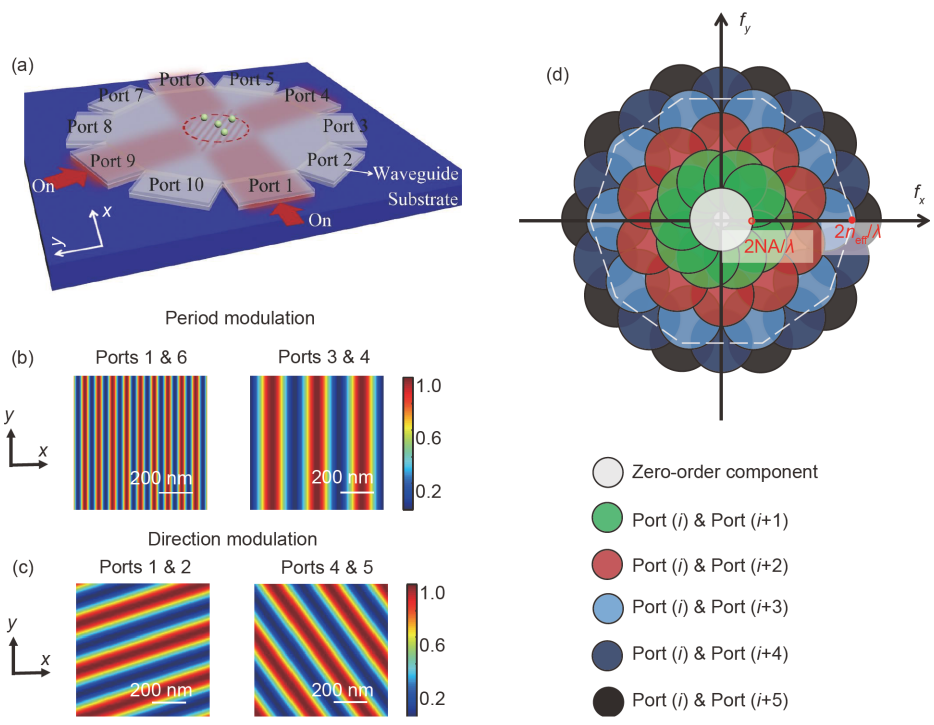

Figure 3 (Color online) Large and tunable SFS of STUN in the lateral dimension. (a) Schematic setup of a STUN chip based on GaP decagon waveguide. The FOV is circled by a red dash line. (b), (c) Examples of the interference patterns with different input ports on, showing the period modulation and direction modulation, respectively. (d) The detected spatial frequency range in STUN. Different colors represent the detectable components with different input ports on. i = 1, 2, 3, 4, 5; λ_{illu} = 561 nm; λ_{emis} = 600 nm; n_{eff} = 3.38; NA = 0.9. Scale bars in (b) and (c): 200 nm.

vector can be actively tuned accordingly to collect all the necessary spatial frequency information. Figure 3(d) shows the spatial frequency spectrum within $(2n_{eff}\cdot\lambda_{emis}/\lambda_{illu}+2NA)/\lambda_{emis}$ can be completely detected in our GaP chip-based STUN model, corresponding to a lateral resolution of $\lambda_{emis}/(2n_{eff}\cdot\lambda_{emis}/\lambda_{illu}+2NA)$.

2.2 SFS tuning in the vertical dimension

The SFS effect in the vertical dimension can be utilized to

achieve superresolution sectioning capability, as illustrated by Figure 4(a). The vertical spatial frequency of the evanescent illumination covers a range much wider than the vertical spatial frequency passband of the objective and is mixed with the spatial frequencies of the object, which provides the basis to achieve the ultra-high resolution in the vertical dimension. Figure 4(b) shows the intensity distribution of the evanescent wave on the GaP waveguide chip, and Figure 4(c) shows its spatial frequency spectrum. The red dot line in Figure 4(c) represents the position of the axial cutoff spatial frequency ($0.56/\lambda$) of a 0.9NA objective. The ultra-wide range of the spatial frequency spectrum shown in Figure 4(c) infers that deep-subwavelength vertical resolution is possible.

Consequently, the high spatial frequency spectrum information in the vertical dimension of the object has been shifted to the passband of the objective by the illumination. To extract the high spatial frequency information of the object, we introduce a sectional saturation effect. The saturation effect is a nonlinear process, which can change the line shape of the vertical intensity distribution of evanescent illumination. It is possible to saturate the surficial fluorophores by increasing the input laser intensity, and in this saturated region, the spatial frequency of the "effective illumination intensity distribution" is down-tuned, as shown by the orange zone in Figure 4(d). The high spatial frequency region is moved away from the surface, which is like a vertical scanning process to enable sectional imaging. The "effective illumination intensity distribution" can be considered as the coefficients in the equation set formed by tens of images captured at different saturation intensities, and the unknown vertical spatial distribution within the penetration depth of the evanescent wave can be solved (sect. 5 in Supplementary Information).

This sectional method has compatibility with chip-based illumination, which is difficult in the commonly used methods that require modulation of the incident angle to the total internal reflection interface [32,33]. Pulsed excitation shorter than the lifetime of fluorophores can be utilized for the sectional saturation effect, promising fast acquisition and low photo-toxicity.

3 Results and analysis

3.1 The lateral resolution of 2D STUN

We performed simulations to illustrate the lateral resolution as well as the FOV. In our simulations, the side length and the thickness of the decagonal GaP waveguide (Figure 3(a)) are designed to be 100 and 250 nm, respectively. The n_{eff} of the TM fundamental mode is 3.38 at a wavelength of 561 nm. Randomly positioned 25-nm-sized fluorescent beads with a 600-nm emission wavelength are used as the object. We use a comparatively low NA of 0.9 to show the benefit of STUN

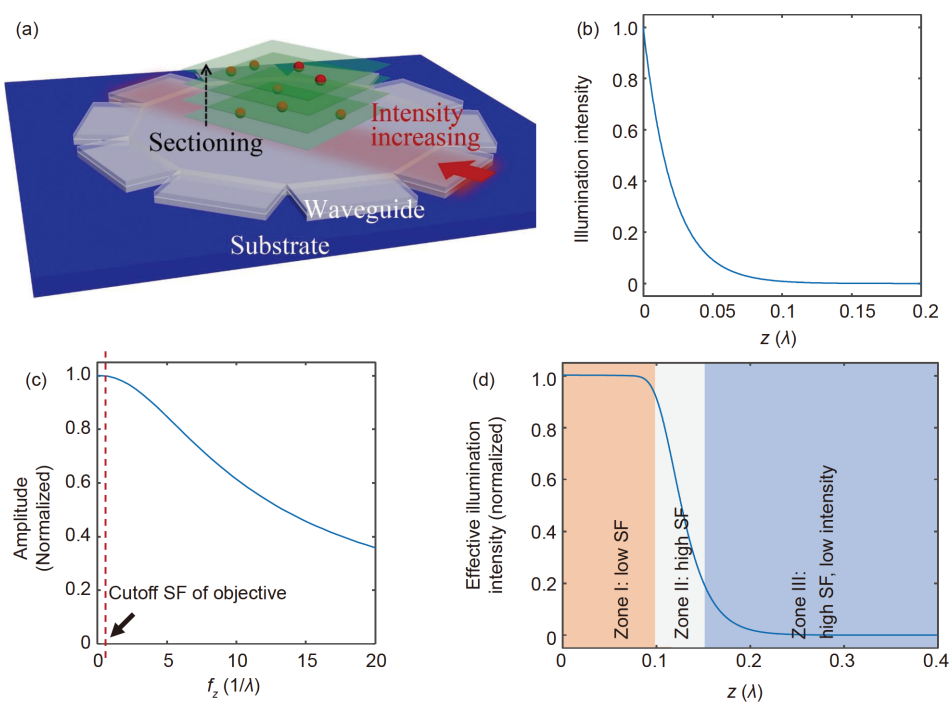

Figure 4 (Color online) Mechanism of the SFS tuning in vertical dimension based on sectional saturation effect for superresolution sectional imaging. (a) The schematic diagram. One port is chosen for input. (b), (c) The exponential intensity distribution of the evanescent wave on a GaP chip and its spatial frequency spectrum. The red dot line represents the position of the axial cutoff spatial frequency (~$0.56/\lambda$) of the objective. (d) Emission intensities (or effective illumination intensities) along the vertical dimension with the surficial objects saturated. Objective NA = 0.9; λ_{illu} = 561 nm; λ_{emis} = 600 nm; SF denotes spatial frequency.

for acquiring both high resolution and large FOV.

Under the illumination scheme defined by the above parameters, the resolution could be improved by 5 folds beyond the Abbe diffraction limit. For each SFS vector used in STUN, three images with different phases are recorded to solve the three components centered at the origin and $\pm\mathbf{f}_{\mathrm{illu}}$ in the spatial frequency domain. We have developed a reconstruction algorithm for STUN to recover the spatial frequency spectrum progressively from the zeroth components to the highest components (sect. 3 in Supplementary Information). Aiming to make the phase modulation more flexible in the future, we randomly set the phases of the evanescent waves in the simulation and resorted to a phase estimation reconstructing algorithm to recover the spatial frequency information [34]. A practical modulation of the phase can be performed outside the chip or by integrating phase modulators on the chip. Figure 5(c) shows the reconstructed STUN image. Compared with that of the wide-field diffraction-limited image (Figure 5(a)) and the classical SIM image (Figure 5(b)), the resolution is dramatically improved by STUN. Two fluorescent beads with a center-to-center distance of 65 nm could be separated, corresponding to a resolution of $\lambda_{\mathrm{emis}}/9$ (Figure 5(d1)).

The tunability of the SFS magnitude is essential for image reconstruction in large-SFS nanoscopy. Otherwise, the missing band in the frequency domain will hinder the adoption of classical correlation-based algorithms from estimating the period, direction, and phases of the illumination patterns, which is necessary for solving and shifting back the high spatial frequency components [35]. Moreover, the spatial frequency band missing generates artifacts and distortions in the reconstructed image, even if the exact SFS is

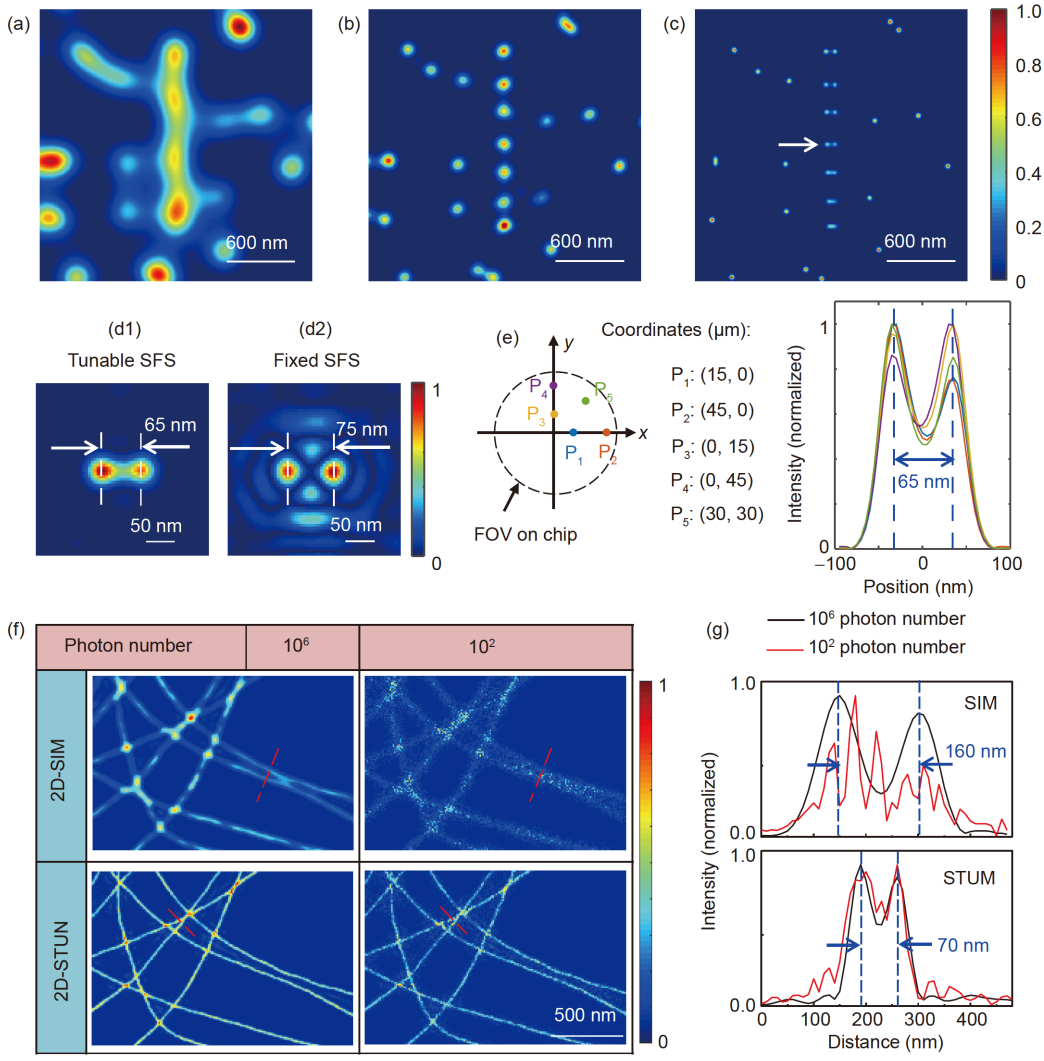

Figure 5 (Color online) Lateral resolution and anti-noise capability of STUN. (a) Wide-field image; (b) SIM image; (c) STUN image; (d) the STUN image (d1) and the image with large but fixed SFS magnitude (d2); (e) imaging intensity profiles of 65-nm-spacing fluorophore pairs located at different positions shown by P_1-P_5 in the 100-μm-diameter FOV (P_1-P_5, unit of the coordinate is μm); (f) SIM and STUN images of the nano-web patterns with the peak photon number decreased from 10^6 to 10^2. The Poisson noises are added correspondingly. (g) Intensity profiles along the red dash lines in (f) which are used to show the anti-noise capability of SIM and STUN to keep their theoretical resolutions. NA = 0.9; n_{eff} = 3.38; λ_{illu} = 561 nm; λ_{emis} = 600 nm.

known. Figure 5(d2) shows a simulated image of a 65-nm-spacing fluorophore pair with the missing band (sect. 2 in Supplementary Information). Compared with that achieved in the tunable case (Figure 5(d1)), the reconstructed image with fixed SFS has the problem of artifacts, as well as distorted peak-to-peak distance (65-nm-spacing shows in the image as 75 nm).

Chip-based STUN is advantageous for achieving a large FOV. Since illumination and detection are decoupled, a low-NA detection objective can be used to achieve a large FOV and high resolution simultaneously. However, non-uniform illumination, which is a common issue in chip-based microscopy due to the mode distribution properties, degrades the image quality and causes problems in image processing. To achieve uniform subwavelength resolution and brightness in a large FOV, we introduced a calibration algorithm to reconstruct the STUN image in the entire illuminated area (sect. 3 in Supplementary Information). By calibrating the frequency component centered at the origin in the frequency domain using the background intensity distributions and calibrating the frequency component centered at $\pm\mathbf{f}_{\mathrm{illu}}$ using the modulation depth distributions, the spatial frequency information was progressively recovered with the SFS magnitude ranging from the lowest to the highest, to reconstruct a deep-subwavelength image with a large FOV and suppressed artifacts. To demonstrate the successful reconstruction in the entire FOV, Figure 5(e) shows 65-nm-spacing fluorophore pairs located at a different position in the FOV, which can all be correctly reconstructed with this calibration algorithm.

The noise would affect the reconstruction process and degrade the resolution and contrast in practice. To investigate the influence of noise on the image reconstruction, we further conducted simulations with Poisson noise added, which is a typical photon noise due to the fundamental (quantum) physics of photon production [36]. The signal-to-noise-ratio (SNR) is equal to the square root of the number of photons.

We have compared the performance of SIM and STUN at the same noise levels, as shown in Figure 5(f). When the peak photon number is set at 10^6 in the raw images (corresponding to a peak SNR of 10^3), both the SIM and STUN methods have good reconstruction results to achieve their theoretical resolutions (~160 nm for SIM; ~70 nm for STUN; see the dark lines in Figure 5(g)). While when the peak photon number decreases to a lower level of 100 (peak SNR = 10), only the STUN keeps its resolving capability to image the 70-nm-separated objects (red lines in Figure 5(g)). The reconstructed results when the peak photon number decreases to as low as 30 (peak SNR = 5.5) are shown in Figure S5(d) in Supplementary Information. It becomes even harder to resolve any details in the SIM image, while the nano-web patterns can still be resolved in STUN. The better anti-noise capability of STUN could be ascribed to that more overlap exists in the spatial frequency domain in STUN, which suppresses the noise in a manner of averaging, and that much more high spatial frequency spectrum is covered in STUN, which obviously increases the image contrast. These characteristics endow STUN with the ability to image an object with a low SNR at the nanoscale. Compared with SIM, the STUN possesses a resolution 2.5 times improved and does not sacrifice the imaging speed, as its good resilience towards the low SNR allows a shorter exposure time of the raw images. The overlap between the shifted components in the spatial frequency domain can be reduced as long as the complete detection in the spatial frequency domain remains to be ensured (as shown in Figure S6). So that the number of raw images decreases to further increase the imaging speed of STUN.

It should be noted that the adoption of image preprocessing method like the Wiener filter will help further improve the immunization to noise. By choosing appropriate parameters of the Wiener filter, the STUN method can work successfully even when the peak SNR is 1 (Figure S7(a) in Supplementary Information).

3.2 Vertical resolution and the 3D STUN imaging

We perform simulations with a nano-web 3D object to demonstrate the 3D imaging capability of STUN (Figure 6(a)). Firstly, we reconstruct the 2D superresolution image and the sectional image separately for the object within the penetration depth of the evanescent illumination (~30 nm). Then the 2D superresolution image is used as a spatial mask to extract the detailed information of the raw saturated sectioning image stack. The 3D superresolution imaging process can be found in Figure S9 in Supplementary Information. Thirty raw images with different excitation intensities well below the damage threshold of *in vivo* biology are used to solve the vertical spatial distribution of 30 layers within the 30 nm penetration depth. Figure 6(b) shows the effective illumination intensities along the vertical axis used in our simulations. The parameters, including absorption cross-section, lifetime, laser intensity, etc., are in sect. 5 in Supplementary Information. Figure 6(c) shows the reconstructed sectional images at three different layers, multiplied by the 2D superresolution mask.

The 3D images have been reconstructed considering two different levels of noise (Poisson noise added in the raw images with the peak photon number of 10^6 and 10^2, respectively), as shown in Figure 6(d) and (e). In the case of 10^2 photon number, a Wiener denoising filter is used to improve the reconstruction quality. The object depth and the reconstructed depth are consistent well in both cases (Figure 6(f)). We have calculated the deviation of the reconstructed depth from the object depth for every pixel in the object. Through a Gaussian fit, we find the vertical localization

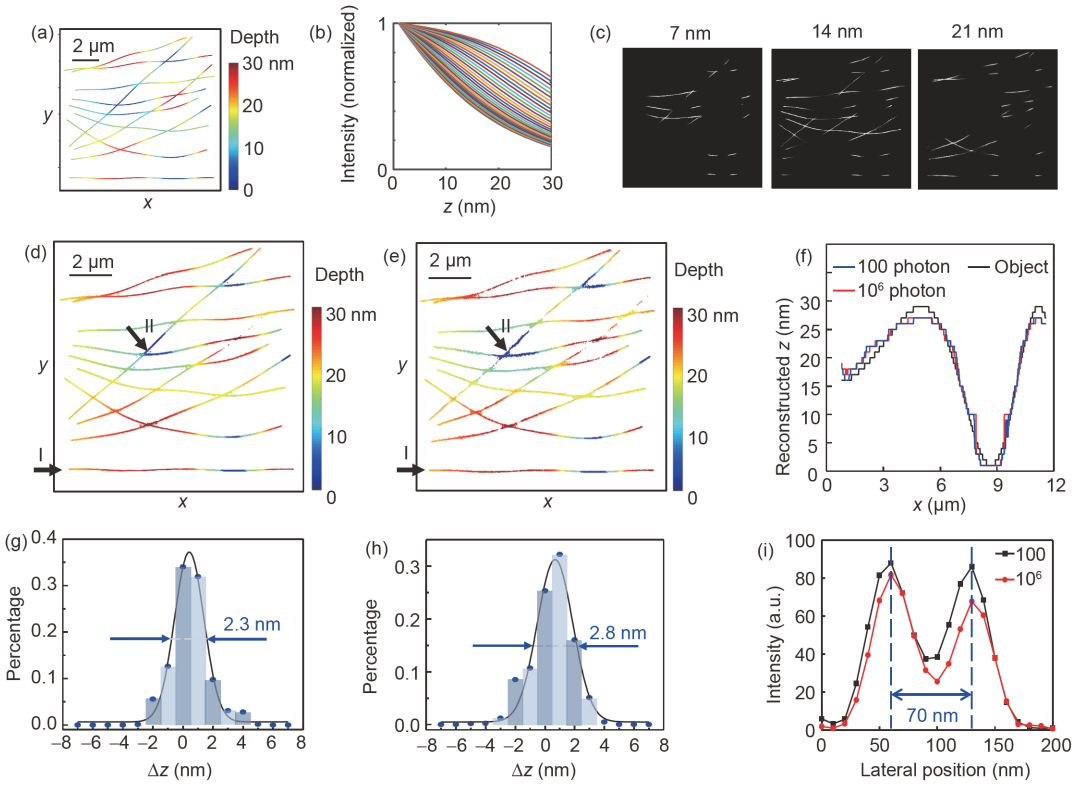

Figure 6 (Color online) 3D STUN imaging. (a) The 3D object used in the simulation. The depth denotes the distance between the object and the waveguide surface. (b) The emission intensity distributions under the 30 different excitation intensities that are used for sectional imaging. (c) Reconstructed superresolution images at three layers with a depth of 7, 14, and 21 nm (noise-free). (d), (e) Reconstructed 3D superresolution image with Poisson noise added. The peak photon number of the raw images is set as 10^6 (d) and 10^2 (e), respectively. (f) The true depth and reconstructed depth of the line-like object pointed by arrow I in (d) and (e). (g), (h) The deviation of the reconstructed depth from the true object depth (Δz), corresponding to the 3D reconstruction results shown in (d) and (e). (i) Intensity profiles corresponding to the position pointed by arrow II in (d) and (e). NA = 0.9; n_{eff} = 3.38; λ_{illu} = 561 nm; λ_{emis} = 600 nm.

precision is better than $\lambda_{\mathrm{emis}}/200$ (Figure 6(g) and (h)). The lateral resolution of the 3D reconstructed image is better than $\lambda_{\mathrm{emis}}/9$, determined by the 2D superresolution mask (Figure 6(i)).

4 Discussion

The highlight of this SFS tuning microscopy method is that the illumination and detection of a wide-field optical system are decoupled not only in configuration but also in function. The high resolution is ensured by the illumination design, circumventing the detection NA. Consequently, we can use a low NA objective in detection for the large FOV without degrading the subdiffraction resolution. The chip can be treated as a compact illumination module, endowing classical microscope with fast, large-FOV, and deep-subwavelength superresolution capability. In the future experiment to promise a mass production, such a GaP waveguide can be fabricated using the III-V hybrid integration process based on direct wafer-bonding followed by electron-beam lithography or photolithography [29,37].

There is no longer a physical limit on the resolution improvement from the Abbe diffraction limit of a linear system. We illustrate a multilayer metamaterial design as an example to show the potential of achieving ultra-deep-subwavelength resolution in 3D (sect. 7 in Supplementary Information). The side view of the multilayer metamaterial-based STUN chip is illustrated in Figure S10(a), which is constituted by SiO_2 substrate-silver (100 nm)-Al_2O_3 (10 nm)-silver (10 nm)-water (sample environment). The substrate is designed to have a thickness to enable the propagation of TM polarized mode, and the 50-nm-width slots are designed for light input, which can compensate for the momentum difference between excitation photons and plasmons. With an excitation wavelength of 520 nm, the FDTD simulations demonstrate that the refractive index of TM mode is 7.2, which is coincide with the 36-nm period of the interference pattern achieved by two opposite ports (Figure S10(b)). The metamaterial chip has been designed to have 12 input ports with different directions to tune the SFS vector for complete spatial frequency spectrum detection (detection NA = 1.49).

Figure S10(c) shows the 3D STUN images based on the metamaterial chip simulated for an object consisting of several nanobeads at a depth of 6 nm. The axial localization precision increases to ~$\lambda/1000$ due to a much higher spatial

frequency that exists vertically compared with that in GaP chip. The statistics data in Figure S10(d) of the reconstructed depth deviation are achieved by simulating images of nanobeads located at various depth within the penetration depth of SPPs. The lateral resolution increases to 30 nm (>λ/18), as demonstrated in Figure S10(e).

The difference between the STUN and the SIM, a very typical SFS based superresolution imaging method, mainly shows in the following aspects. (1) In SIM, the illumination wave vector is determined by the NA of the illumination objective, while in STUN, the lateral wave vector is determined by the much higher effective refractive index of the designed chip, and thus the lateral resolution can be greatly enhanced. (2) In SIM, only the orientation of the illumination pattern is scanned. While in STUN, both orientation and period of the illumination patterns are scanned to completely cover a range in the spatial frequency domain much larger than the passband of the objective (Figure 3(d)). (3) In 3D SIM, the SFS in the axial dimension is determined by a real wave vector, while in STUN, the ultra-high SFS exists in the axial dimension owing to the exponential intensity distribution of the evanescent wave with an imaginary wave vector.

It is noteworthy that this tuning mechanism only works for fluorescent samples. For the scattering sample, the SFS value can be tuned by generating evanescent illumination with different transverse wave vectors, for example using different illumination wavelengths [13,14]. Another concern regarding the method is that, although resolution can be improved by increasing the effective refractive index of the chip, the resultant shallower field penetration depth would limit the capability for volumetric imaging. Thus the resolution and imaging depth need to be designed together according to the specific application. An advantage of the shallow illumination depth is that the defocus noise could be cut down, making the STUN suitable for imaging structures located in the vicinity of the STUN chip surface, for example, the cell membrane.

The imaging speed is critical, especially in studying dynamic biological activities, which is positively associated with the anti-noise capability of the imaging method, the emitter density, the illumination intensity, as well as the objective collection efficiency. In the case of 2D STUN imaging with GaP waveguide chip and 0.9NA objective, 75 raw images at most are taken, and the peak photon number of 10 in one pixel (10 nm×10 nm) in each raw image is sufficient for reconstruction. Let's assume that 40 fluorescent molecules/(10 nm×10 nm×10 nm) are labeled on a 10-nm-thick wire-like object; the absorption cross-section of the fluorophore is ~10^{-16} cm^2; the illumination intensity is 100 W/cm^2, then ~1 ms exposure time is required to capture one raw image with a peak photon number of ~30 to ensure the correct reconstruction (Figure S5(d)). Consequently, an imaging speed of ~10 Hz is possible for 2D STUN imaging. The number of photons emitted by one fluorescent molecule is ~2000 for one reconstructed 2D STUN image. For 3D STUN imaging, another 30 images are taken under pulsed laser illumination of various intensities to extract the depth information. To ensure the peak photon number of ~100 in each raw image (assuming the repetition rate of illumination laser is 10 kHz), the exposure time is ~30 ms, and thus the 3D STUN imaging speed would be ~1 Hz. It is noteworthy that biological fluorophores may bleach in the 3D STUN because each fluorophore emits ~10^4 photons for one reconstructed 3D image. The 2D STUN with lateral superresolution is more suitable for the large-FOV, dynamical observation of biological samples. The 3D STUN can be used with advanced materials, such as vacancy centers in diamond, for sensing with nanoscale resolution [38].

5 Conclusion and outlook

In this article, a chip-compatible 3D nanoscopy called STUN is introduced. By combining the SFS tunability with the evanescent wave illumination of large and imaginary wave vectors, a deep-subwavelength 3D superresolution image can be achieved without distortion. This STUN method has solved a significant challenge in current 3D superresolution microscopy by providing a nanoscopy with deep-subwavelength resolutions, large FOV, and high speed simultaneously. The 3D superresolution imaging results based on a GaP chip waveguide demonstrate a resolution of ~70 nm laterally and ~3 nm vertically. The position of each detected circular sub-range in the spatial frequency domain can be actively determined by selecting which input ports on, and the redundant overlap can be suppressed to further increase the imaging speed. By comparing STUN and SIM, we find the STUN shows a much better resolution and a more excellent anti-noise capability. Metamaterials with unusual refractive indexes could potentially be introduced to combine with the tunable SFS effect for molecular-scale visualization. In short, this study offers a new method of mass-producible, easily-integrated, and high-throughput nanoscopy, which could benefit life science research, biomedicine, and material science, among others.

This work was supported by the National Natural Science Foundation of China (Grant Nos. 61735017, 61822510, 62020106002, 61905097, and 62005250), the Zhejiang Provincial Natural Science of China (Grant No. LR17F050002), and the Zhejiang University Education Foundation Global Partnership Fund. We thank Drs. Qiulan Liu, Ruizhi Cao, and Wenjie Liu for the discussion on the details of the superresolution imaging reconstruction.

Supporting Information

The supporting information is available online at http://phys.scichina.com and https://link.springer.com. The supporting materials are published as

submitted, without typesetting or editing. The responsibility for scientific accuracy and content remains entirely with the authors.

1 T. A. Klar, S. Jakobs, M. Dyba, A. Egner, and S. W. Hell, Proc. Natl. Acad. Sci. USA **97**, 8206 (2000).
2 E. Rittweger, K. Y. Han, S. E. Irvine, C. Eggeling, and S. W. Hell, Nat. Photon. **3**, 144 (2009).
3 E. Betzig, G. H. Patterson, R. Sougrat, O. W. Lindwasser, S. Olenych, J. S. Bonifacino, M. W. Davidson, J. Lippincott-Schwartz, and H. F. Hess, Science **313**, 1642 (2006).
4 X. Zhuang, Nat. Photon. **3**, 365 (2009).
5 F. Balzarotti, Y. Eilers, K. C. Gwosch, A. H. Gynnå, V. Westphal, F. D. Stefani, J. Elf, and S. W. Hell, Science **355**, 606 (2017), arXiv: 1611.03401.
6 Y. Eilers, H. Ta, K. C. Gwosch, F. Balzarotti, and S. W. Hell, Proc. Natl. Acad. Sci. USA **115**, 6117 (2018).
7 W. Yu, B. Guo, H. Zhang, J. Zhou, X. Yu, L. Zhu, D. Xue, W. Liu, X. Sun, and J. Qian, Sci. Bull. **64**, 410 (2019).
8 G. Zhao, C. Zheng, C. Kuang, R. Zhou, M. M. Kabir, K. C. Toussaint, W. Wang, L. Xu, H. Li, P. Xiu, and X. Liu, Phys. Rev. Lett. **120**, 193901 (2018).
9 C. Chen, F. Wang, S. Wen, Q. P. Su, M. C. L. Wu, Y. Liu, B. Wang, D. Li, X. Shan, M. Kianinia, I. Aharonovich, M. Toth, S. P. Jackson, P. Xi, and D. Jin, Nat. Commun. **9**, 3290 (2018).
10 M. Tang, X. Liu, Z. Wen, F. Lin, C. Meng, X. Liu, Y. Ma, and Q. Yang, Laser Photon. Rev. **14**, 1900011 (2020).
11 A. Classen, J. von Zanthier, M. O. Scully, and G. S. Agarwal, Optica **4**, 580 (2017), arXiv: 1702.04319.
12 L. Shao, P. Kner, E. H. Rego, and M. G. L. Gustafsson, Nat. Methods **8**, 1044 (2011).
13 X. Liu, C. Kuang, X. Hao, C. Pang, P. Xu, H. Li, Y. Liu, C. Yu, Y. Xu, D. Nan, W. Shen, Y. Fang, L. He, X. Liu, and Q. Yang, Phys. Rev. Lett. **118**, 076101 (2017).
14 C. Pang, J. Li, M. Tang, J. Wang, I. Mela, F. Ströhl, L. Hecker, W. Shen, Q. Liu, X. Liu, Y. Wang, H. Zhang, M. Xu, X. Zhang, X. Liu, Q. Yang, and C. F. Kaminski, Adv. Funct. Mater. **29**, 1900126 (2019).
15 H. S. Li, P. Fan, H. Xia, H. Peng, and G. L. Long, Sci. China-Phys. Mech. Astron. **63**, 280311 (2020).
16 T. Li, Sci. China-Phys. Mech. Astron. **63**, 284231 (2020).
17 Ø. I. Helle, F. T. Dullo, M. Lahrberg, J. C. Tinguely, O. G. Hellesø, and B. S. Ahluwalia, Nat. Photon. **14**, 431 (2020), arXiv: 1903.05512.
18 O. Mudanyali, E. McLeod, W. Luo, A. Greenbaum, A. F. Coskun, Y. Hennequin, C. P. Allier, and A. Ozcan, Nat. Photon. **7**, 247 (2013).
19 X. Qiang, X. Zhou, J. Wang, C. M. Wilkes, T. Loke, S. O'Gara, L. Kling, G. D. Marshall, R. Santagati, T. C. Ralph, J. B. Wang, J. L. O'Brien, M. G. Thompson, and J. C. F. Matthews, Nat. Photon. **12**, 534 (2018), arXiv: 1809.09791.
20 M. Tang, P. Xu, Z. Wen, X. Chen, C. Pang, X. Xu, C. Meng, X. Liu, H. Tian, N. Raghavan, and Q. Yang, Sci. Bull. **63**, 1118 (2018).
21 X. Hao, X. Liu, C. Kuang, Y. Li, Y. Ku, H. Zhang, H. Li, and L. Tong, Appl. Phys. Lett. **102**, 013104 (2013).
22 C. Pang, X. Liu, M. Zhuge, X. Liu, M. G. Somekh, Y. Zhao, D. Jin, W. Shen, H. Li, L. Wu, C. Wang, C. Kuang, and Q. Yang, Opt. Lett. **42**, 4569 (2017).
23 X. Zeng, Z. Liao, M. Al-Amri, and M. S. Zubairy, Phys. Rev. A **91**, 063811 (2015).
24 S. Cao, T. Wang, J. Yang, B. Hu, U. Levy, and W. Yu, Sci. Rep. **7**, 1328 (2017).
25 S. Cao, T. Wang, Q. Sun, B. Hu, U. Levy, and W. Yu, Opt. Express **25**, 14494 (2017).
26 F. Wei, D. Lu, H. Shen, W. Wan, J. L. Ponsetto, E. Huang, and Z. Liu, Nano Lett. **14**, 4634 (2014).
27 A. Bezryadina, J. Zhao, Y. Xia, X. Zhang, and Z. Liu, ACS Nano **12**, 8248 (2018).
28 D. E. Aspnes, and A. A. Studna, Phys. Rev. B **27**, 985 (1983).
29 D. J. Wilson, K. Schneider, S. Hönl, M. Anderson, Y. Baumgartner, L. Czornomaz, T. J. Kippenberg, and P. Seidler, Nat. Photon. **14**, 57 (2019), arXiv: 1808.03554.
30 M. Anitei, and B. Hoflack, Nat. Cell Biol. **14**, 11 (2012).
31 Z. Chen, and S. L. Schmid, J. Cell Biol. **219**, e202005126 (2020).
32 J. Boulanger, C. Gueudry, D. Münch, B. Cinquin, P. Paul-Gilloteaux, S. Bardin, C. Guérin, F. Senger, L. Blanchoin, and J. Salamero, Proc. Natl. Acad. Sci. USA **111**, 17164 (2014).
33 Y. Chen, W. Liu, Z. Zhang, C. Zheng, Y. Huang, R. Cao, D. Zhu, L. Xu, M. Zhang, Y. H. Zhang, J. Fan, L. Jin, Y. Xu, C. Kuang, and X. Liu, Nat. Commun. **9**, 4818 (2018).
34 R. Cao, Y. Chen, W. Liu, D. Zhu, C. Kuang, Y. Xu, and X. Liu, Biomed. Opt. Express **9**, 5037 (2018).
35 A. Lal, C. Shan, and P. Xi, IEEE J. Sel. Top. Quantum Electron. **22**, 50 (2016), arXiv: 1602.06904.
36 Q. Zhao, I. T. Young, and J. G. S. de Jong, J. Biomed. Opt. **16**, 086007 (2011).
37 M. Wang, R. Wu, J. Lin, J. Zhang, Z. Fang, Z. Chai, and Y. Cheng, Quantum Eng. **1**, e9 (2019).
38 J. M. Taylor, P. Cappellaro, L. Childress, L. Jiang, D. Budker, P. R. Hemmer, A. Yacoby, R. Walsworth, and M. D. Lukin, Nat. Phys. **4**, 810 (2008), arXiv: 0805.1367.